

Broadband and parallel multiple-order optical spatial differentiation enabled by Bessel vortex modulated metalens

Received: 8 May 2024

Accepted: 14 October 2024

Published online: 19 October 2024



Pengcheng Huo^{1,2,5}, Le Tan^{1,3,5}, Yaqi Jin^{1,5}, Yanzeng Zhang¹, Mingze Liu¹,
Peicheng Lin¹, Song Zhang¹, Yilin Wang¹, Haiyang Ren¹, Yanqing Lu^{1,2}✉ &
Ting Xu^{1,2,4}✉

Optical analog image processing technology is expected to provide an effective solution for high-throughput and real-time data processing with low power consumption. In various operations, optical spatial differential operations are essential in edge extraction, data compression, and feature classification. Unfortunately, existing methods can only perform low-order or selectively perform a particular high-order differential operation. Here, we propose and experimentally demonstrate a Bessel vortex modulated metalens composed of a single complex amplitude metasurface, which can perform multiple-order radial differential operations over a wide band by presetting the order of the corresponding Bessel vortex. This architecture further enables angle multiplexing to create multiple information channels that synchronously perform multi-order spatial differential operations, indicating the superiority of the proposed devices in parallel processing. Our approach may find various applications in artificial intelligence, machine vision, autonomous driving, and advanced biomedical imaging.

Signal and image processing techniques based on integrated electric circuits suffer from speed and power consumption constraints in high-throughput data processing applications. All-optical computation is referred to as an effective alternative because of its excellent ability to implement massive parallel processing with high speed and low power consumption. As one of the most essential mathematical operations, optical analog spatial differential processing has attracted particular attention in the past few years^{1–7}. It can realize real-time data compression and feature classification by extracting the edge information of the objects and, therefore, shows essential application value in highly sophisticated fields such as artificial intelligence, machine vision, autonomous driving, and biomedical imaging^{8–13}. Unfortunately, conventional optical differential systems in the spatial and

temporal domains are always composed of bulky optical components, leading to difficulties in precise alignment and high-density optical integration^{14–18}.

In recent years, with the rapid development of nanotechnology, various nanophotonic materials have helped construct more compatible and compact optical differential processing systems to address these problems^{19–23}. In particular, metasurfaces, as a periodic two-dimensional array of sub-wavelength artificial scatters, offer great flexibility for precise manipulation of the phase, amplitude, polarization, and frequency of incident light, thereby opening up many opportunities to this field with significant advantages^{24–31}. Up to this point, most planar meta-optics have been limited to low-order differential operations, such as the first-

¹National Laboratory of Solid-State Microstructures, College of Engineering and Applied Sciences, and Collaborative Innovation Center of Advanced Microstructures, Nanjing University, 210093 Nanjing, China. ²Key Laboratory of Intelligent Optical Sensing and Manipulation, Nanjing University, 210093 Nanjing, China. ³School of Electronic Science and Engineering, Nanjing University, 210093 Nanjing, China. ⁴School of Materials Engineering, Jiangsu University of Technology, 213001 Changzhou, China. ⁵These authors contributed equally: Pengcheng Huo, Le Tan, Yaqi Jin. ✉e-mail: yqlu@nju.edu.cn; xuting@nju.edu.cn

or second-order^{14–24,32–46}. Based on the nonlocality of the dielectric multilayer, a multiple-order analog spatial differentiator is proposed to realize some higher-order differential operations, such as the third- or fourth-order⁴⁷. The device offers significant advantages in terms of low-complex fabrication and low sensitivity to misalignment. However, this approach limits the broadband expansion and parallel processing capabilities of optical computations. In fact, the ability to synchronously perform multiple-order differential operations on a single device over a wide band is essential for large-scale optical data processing, but unfortunately, it remains a significant challenge.

In this paper, we propose a compact platform based on a single-layer complex amplitude metasurface for multiple-order spatial differentiation across the visible region. By introducing the modulation of the Bessel vortex on the metalens, the coherent transfer function (CTF) of the device shows an exponential correlation with the order of the Bessel vortex, enabling the same order differential operation as the topological charge. As a proof-of-concept, we experimentally demonstrate the isotropic differential processing capability of the first- to fourth-order Bessel vortex modulated metalens (BVML), with the potential for unlimited orders in principle. Thanks to the wavelength insensitivity of the Pancharatnam-Berry (PB) phase employed in the metasurface design, the fabricated devices exhibit broadband response. Furthermore, to maximize the parallel processing advantages of optical computing, synchronous multiple-order radial differential operations are implemented by angle multiplexing on a single metasurface. This platform has the potential to significantly advance the field of optical analog processing, as

well as contribute to the progress of artificial intelligence and biomedical imaging.

Results

Theory and principle

To achieve multiple-order two-dimensional spatial differentiation, we start by considering the BVML with rotational symmetry as schematically illustrated in Fig. 1a. Under coherent illumination, the incident light field E_{in} is modulated by the CTF of the metalens, and different optical differential processing results E_{out} are output on the image plane, which is determined by the order of the Bessel vortex. The BVML is designed to be integrated on a single-layer metasurface containing the complex amplitude of a Bessel vortex and the complex amplitude of a focusing lens, as shown in Fig. 1b. Therefore, the complex transmission coefficient of the BVML in polar coordinates (r, φ) can be described as follows:

$$M_l(r, \varphi) = J_l(\alpha r) \exp(i l \varphi) \cdot \exp\left(-i k_0 \frac{r^2}{2f}\right) \quad (1)$$

where l is the topological charge of the vortex, $k_0 = 2\pi/\lambda$ is the free-space wavenumber, λ is the free-space wavelength, and f denotes the focal length of metalens. The function $J_l(\cdot)$ refers to the l th-order Bessel function of the first kind. The coefficient α is defined as $\xi_{n,l}/R$, where R and $\xi_{n,l}$ denote the radius of the metalens and the n th zero of the corresponding l th-order Bessel function, $J_l(\xi_{n,l}) = 0$. Based on the Fresnel diffraction approximation, the point spread function (PSF) of the BVML in polar coordinates (ρ, ϕ) on the back

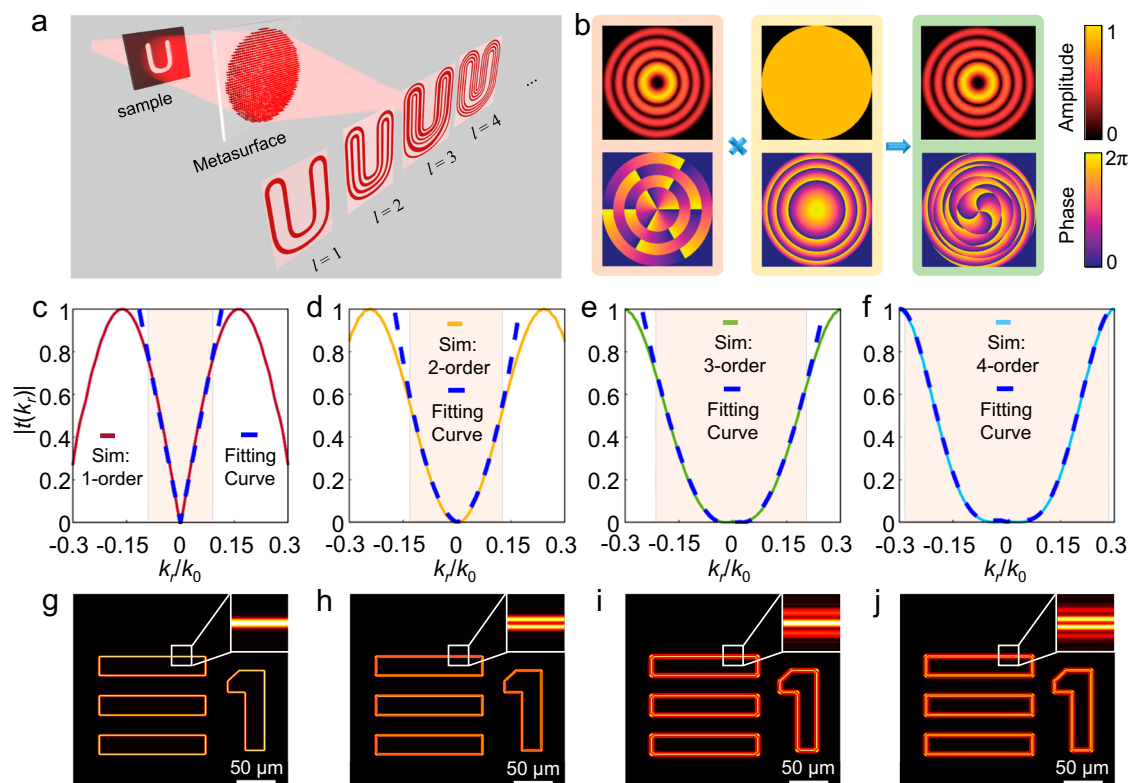


Fig. 1 | Working principle of the BVML for multiple-order radial differential operations. **a** Schematic of the proposed BVML based on a dielectric metasurface. The metasurface device modulates the incident object light field and outputs a l th-order differential image at the imaging plane according to the order of the Bessel vortex encoded in its profile. **b** Amplitude and phase distributions of the BVML combining a Bessel vortex and a focusing lens. **c–f** Simulated CTF curves for the

first-, second-, third-, and fourth-order BVMLs and the corresponding fitting curves using the form $|t(k_r)| = a|k_r|^l$. The abbreviation “Sim” has the full name of “Simulation”. **g–j** Simulated differential processing results of the first-, second-, third-, and fourth-order BVMLs. The input object is part of the 1951 USAF test chart. The enlarged insets highlight the number of edges. Scale bars: 50 μm .

focal plane can be obtained as (see Supplementary Section 1 for details),

$$h_l(\rho, \phi) = \frac{(-i)^{l+1}}{\alpha f} \exp\left(ik_0\left(\frac{\rho^2}{2f} + f\right) + il\phi\right) \delta\left(\frac{k_0}{f}\rho - \alpha\right) \quad (2)$$

According to the Fourier transform relation, the CTF of the BVML in the spatial frequency domain can be derived as $t_l(k_r) = \mathcal{F}\{h_l(\rho, \phi)\} \propto J_l(\alpha f k_r / k_0)$, where $k_r = (k_x^2 + k_y^2)^{1/2}$ refers to the in-plane wavevector along the radial direction. For any non-negative integer l , the asymptotic behavior of the Bessel function with near-zero variable further ensures that the CTF fundamentally satisfies the form of $t_l(k_r) \propto (\alpha f k_r / k_0)^l$. Therefore, based on the correspondence between the spatial differential operator ($\partial/\partial r$) and the transfer function (k_r^l), the designed BVMLs show the

ability to perform multiple-order radial differential operations ($E_{\text{out}} \propto \partial^l E_{\text{in}} / \partial r^l$) in the polar coordinate system by presetting the topological charge of the corresponding Bessel vortex, which enable two-dimensional optical analog signal processing.

Figure 1c–f presents the simulated CTF curves of the first- to fourth-order BVMLs, respectively. The corresponding fitted curves verify that the CTF has the form of k_r^l around $k_r = 0$, which is consistent with the theoretical prediction above. Then, we simulate the first- to fourth-order spatial differential processing of the optical image using the designed BVML, as shown in Fig. 1g–j. The edges of the output images are presented clearly along both the horizontal and vertical directions, thus indicating the two-dimensional processing effect. In the partially enlarged detail views of the inset of each panel, the number of edges that can be visually distinguished also represents the typical nature of the l th-order derivative processing.

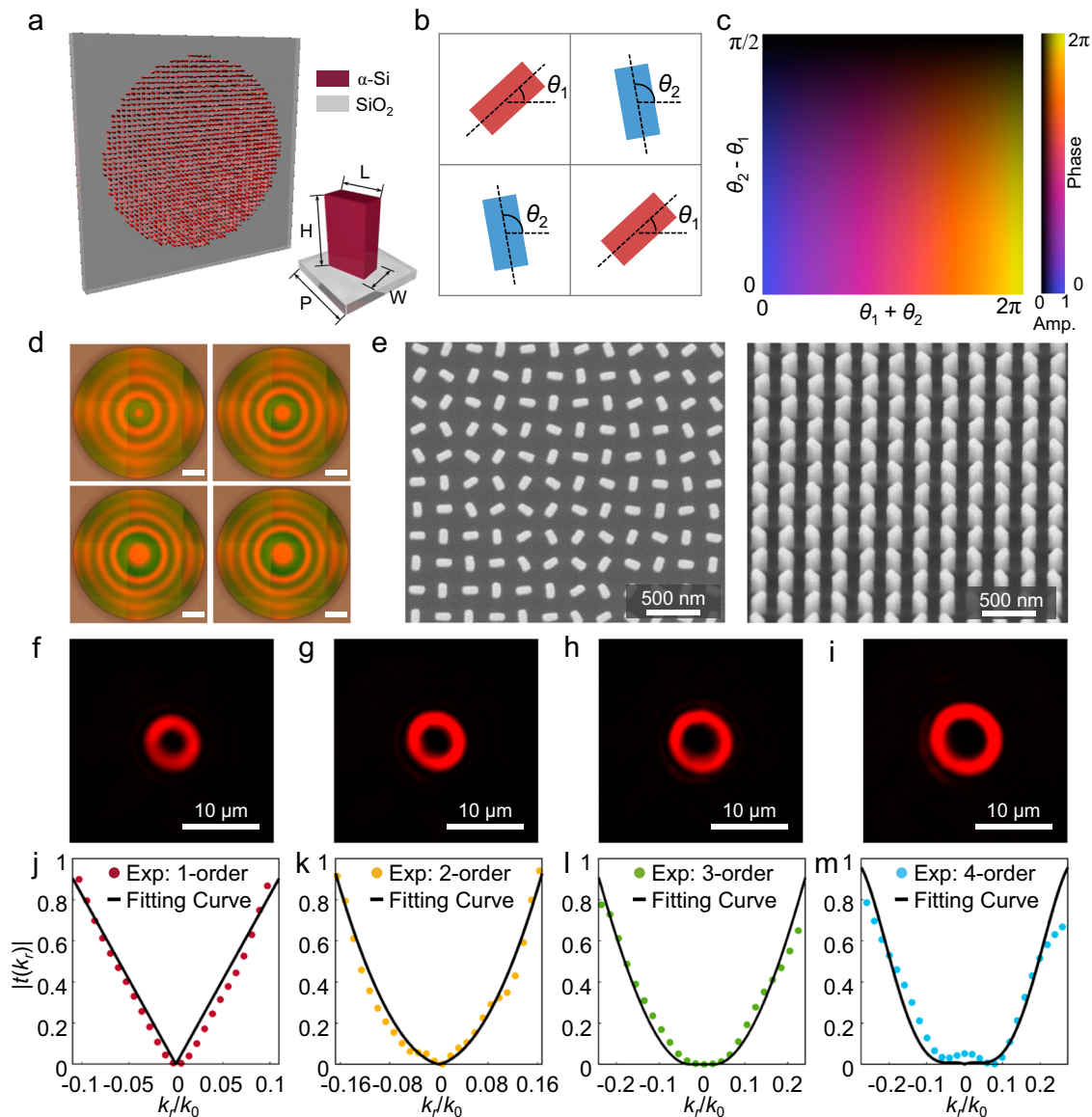


Fig. 2 | The BVML design and characterization. **a** Schematic of the designed metasurface. Unit cell structure is composed of rectangular shaped α -Si nanopillars on a SiO_2 substrate, with the long axis $L = 150$ nm, the short axis $W = 80$ nm, the height $H = 400$ nm, and the period $P = 250$ nm. **b** Schematic top view of the superpixel realizing complex amplitude modulation. **c** The complex amplitude value as the function of the rotation angles of the two groups of nanopillars in the superpixel. The abbreviation “Amp.” has the full name of “Amplitude”. **d** The optical

photographs of the fabricated metasurfaces corresponding to the first- to fourth-order BVMLs, respectively. Scale bars: 200 μm . **e** Top and tilted views of the SEM images of the α -Si nanopillar arrays. Scale bars: 500 nm. **f–i** Experimentally measured PSF of the first- to fourth-order BVMLs at the wavelength of 633 nm. Scale bars: 10 μm . **j–m** The experimental CTF curves for these BVMLs extracted from (f–i), respectively, and fitted by the corresponding order polynomial. The abbreviation “Exp” has the full name of “Experiment”.

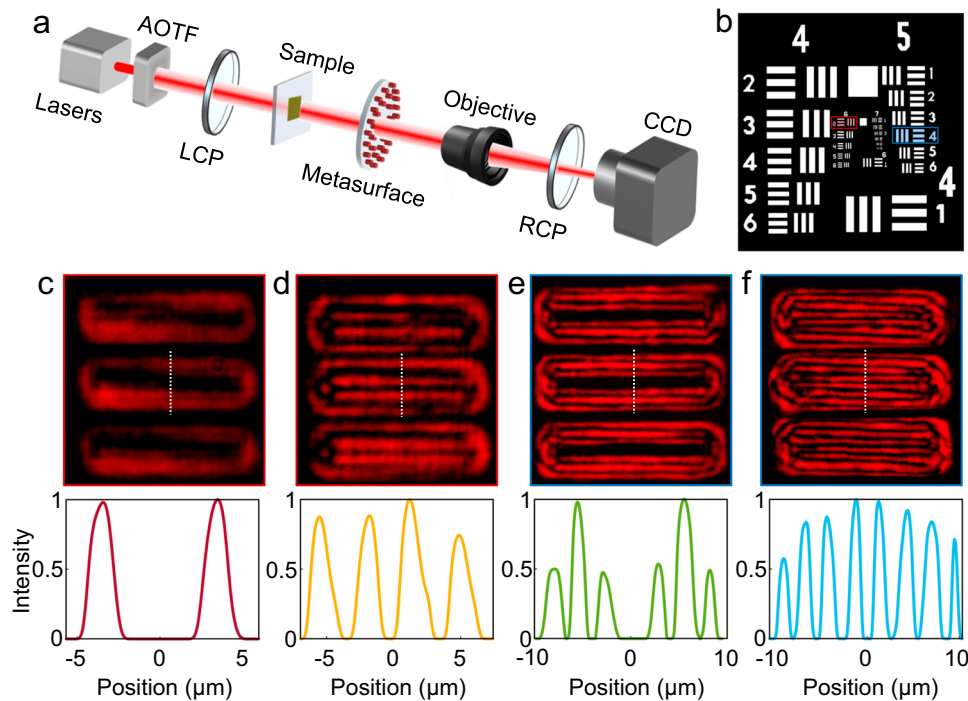


Fig. 3 | Resolution testing of the BVMLs. **a** Schematic of the experimental setup used to perform different order radial differential processing. **b** The standard 1951 USAF resolution test chart as the input object. **c, d** Imaging results of the test target 6-2 marked by the red box in **(b)** through the first- and second-order BVMLs.

e, f Imaging results of the test target 5-4 marked by the blue box in **(b)** through the third- and fourth-order BVMLs. Each lower panel of **(c–f)**: the normalized intensity distribution along the corresponding vertical dashed line.

Design and fabrication of BVML

The proposed BVML is a single-layer metasurface consisting of an array of rectangular-shaped amorphous silicon (α -Si) nanopillars with a height of 400 nm and a subwavelength period of 250 nm on the fused-silicon substrate, as shown in Fig. 2a. The nanopillar is optimized to be 80 nm in width and 150 nm in length, acting as a nanoscale half-wave plate (HWP) with high polarization conversion efficiency in the visible range (see Supplementary Section 2 and 3 for details). For a left-handed circularly polarized (LCP) incident light, the transmitted light with opposite chirality has a PB geometric phase factor $\exp(i2\theta)$, where θ is the in-plane rotation angle of the nanopillar concerning the fast axis^{24–31}. To implement a complex amplitude modulation on the incident light²⁸, we arrange two groups of nanopillars alternately in a square lattice to form a super-pixel, as depicted in Fig. 2b. According to the interference principle, the transmitted field can be simplified as $\cos(\theta_2 - \theta_1)\exp(i(\theta_1 + \theta_2))$, where θ_1 and θ_2 are the rotation angles of the two groups of nanopillars respectively (see Supplementary Section 4 for details). Thus, a continuous smooth amplitude distribution from 0 to 1 and phase distribution from 0 to 2π can be achieved independently by simply changing the orientation angle of the nanopillars, as shown in Fig. 2c. Based on the above principle, the target complex amplitude $E\exp(i\psi)$ of the designed BVML (Fig. 1b) can be encoded into the single-layer metasurface by using the following relationship,

$$\theta_1 = \frac{\psi - \cos^{-1}(E)}{2}, \theta_2 = \frac{\psi + \cos^{-1}(E)}{2} \quad (3)$$

Figure 2d, e depicts the optical photographs of the fabricated first- to fourth-order BVMLs and the scanning electron microscope (SEM) images of the α -Si nanopillar array, respectively. The detailed fabrication process is described in the Methods section. All fabricated metasurfaces have a diameter of 1.2 mm and a focal length of 1.2 mm. Figure 2f–i presents the measured PSFs of the first- to fourth-order BVMLs for LCP

incident light with the wavelength of $\lambda = 633$ nm, all of which possess a donut-shaped intensity profile attributed to the orbital angular momentum (OAM) imparted by Bessel vortex. The radius of the ring gradually increases with the value of topological charges. The experimental CTF curves along the radial direction for these BVMLs are extracted from the Fourier transform of PSFs and fitted by the corresponding order polynomial, as shown in Fig. 2j–m. The consistency between the experimental and fitting curves is sufficient to meet the requirements of the devices to perform radial differential operations, as predicted by the theoretical analysis and numerical simulation.

Experimental characterization of BVML

The meticulous design of the experimental setup for multiple-order radial differential processing is schematically illustrated in Fig. 3a. The input image is placed at the object plane of the BVML, illuminated by a coherent light beam generated from a supercontinuum laser attached to an acousto-optic tunable filter (AOTF). A left-handed circular polarizer converts the incident light from linear polarization to fully circular polarization. The spatial differential image output from the BVML is collected with a 50x microscope objective and then captured by the charge-coupled-device (CCD) camera located at the rear focal plane. In order to eliminate background light that is co-polarized with the incident beam and improve the contrast, a right-handed circular polarizer is placed before the CCD.

First, we perform the experiment with the standard 1951 United States Air Force (USAF) resolution test chart as an input object to evaluate the imaging performance of the proposed BVMLs. Figure 3b provides the image of groups 4 to 7 in the resolution test chart, while the colored boxes indicate the test targets of the experiment. Figure 3c–f shows the differential images of the first- and second-order BVMLs for the test target 6-2 (red box in Fig. 3b) and of the third- and fourth-order BVMLs for the test target 5-4 (blue box in Fig. 3b), corresponding to the spatial resolution of 6.96 μm and 11.05 μm , respectively. Here, the higher-order differential operations tend to

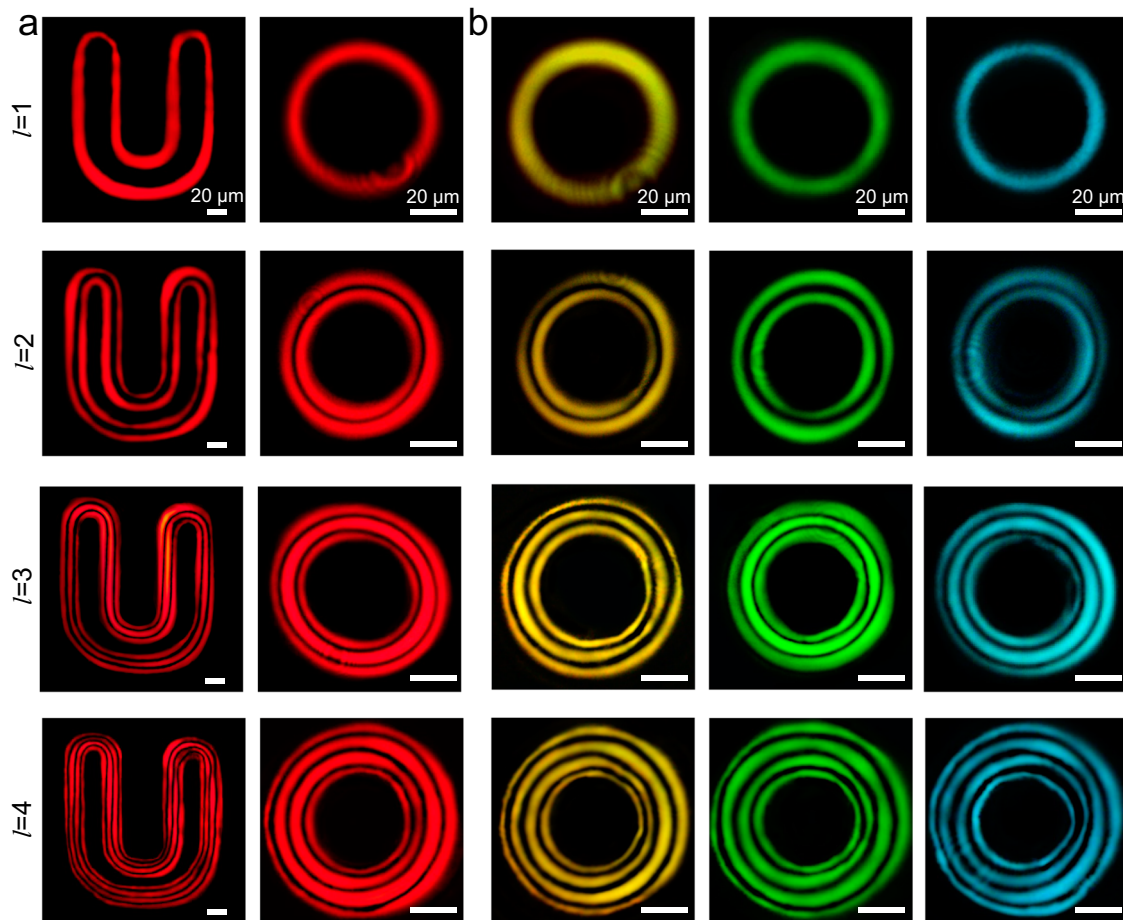


Fig. 4 | Experimental broadband differential imaging results of amplitude objects. **a** The first- to fourth-order differential imaging results of the U-shaped and circular objects at the wavelength of 633 nm. Scale bars: 20 μm . **b** The first- to

fourth-order differential imaging results of the circular object at the wavelengths of 580, 532, and 490 nm, respectively. Scale bars: 20 μm .

have lower resolution, which is consistent with the increasing trend of the PSF size along with the topological charge number of the vortex. Moreover, the resolution of BVMLs is also limited by the maximum spatial frequency of the objects that the metasurface can process. In principle, this resolution can be further improved by reducing the unit structure period and increasing the effective numerical aperture (NA) of the metalens. Each lower panel of Fig. 3c–f shows the normalized intensity distribution along the corresponding vertical dashed lines. As expected, we indeed observe that l peaks show at the edge of the image when l th-order spatial differentiation is performed. The experimental measurements are in good agreement with the numerical results in terms of peak position and number.

Next, we experimentally verify the two-dimensional and broadband response of the radial differential operations performed by the proposed BVMLs. We choose a U-shaped and a circular aperture (Fig. S7) as two different amplitude objects to insert into the optical system. The corresponding outputs of the first- to fourth-order differential images under coherent illumination at the wavelength of 633 nm are presented in Fig. 4a. As expected, the step edges of the amplitude are enhanced along all directions and split into the typical l edges. The uniform edge intensity distribution in all images, especially the symmetry in every order differential image of circular aperture object, indicates that the proposed BVMLs have excellent capability of performing isotropic radial differential processing, whose order is determined by the topological charge of the Bessel vortex applied to the metalens. Furthermore, by changing the filtered output of the laser via adjusting the AOTF, we also record the first- to fourth-order differential results of circular aperture at the wavelengths of 580 nm,

532 nm, and 490 nm, respectively, as shown in Fig. 4b. The consistency of the output at different wavelengths reveals that the geometric phase metasurfaces can ultimately enable the designed BVMLs to perform multiple-order differential processing over a broad spectrum.

Multichannel parallel processing using BVML

To verify the superiority of the proposed BVMLs in parallel multichannel image processing, Fig. 5a presents a schematic illustration of synchronous multi-order radial differential operations using metasurface under coherent light illumination. Here, the metasurfaces enable angle multiplexing to create multiple independent information channels that perform the zeroth- to fourth-order spatial differential operations in a single shot. In principle, there is no limit to the number of channels. Figure 5b shows the design schematic, where the complex amplitude profile of the zeroth- to fourth-order BVMLs is superimposed with different deflection phase profiles, respectively, forming a multichannel metalens. The focal-spot position is controlled by angular multiplexing, with each angle corresponding to a specific order. The analytical expression of the complex amplitude profile multiplexing all channels is given by

$$M(r, \varphi) = \sum_{l=0}^N \{M_l(r, \varphi) \cdot \sqrt{\omega_l} \exp(ik_0 r \sin(\phi_l) \cos(\varphi - \phi_l))\} \quad (4)$$

where $M(r, \varphi)$ is a complex amplitude field. Also, N denotes the total number of channels in the designed device; $M_l(r, \varphi)$ denotes the complex amplitude of the l th-order BVML applied to the l th channel; ω_l is the corresponding weight of each channel, which is

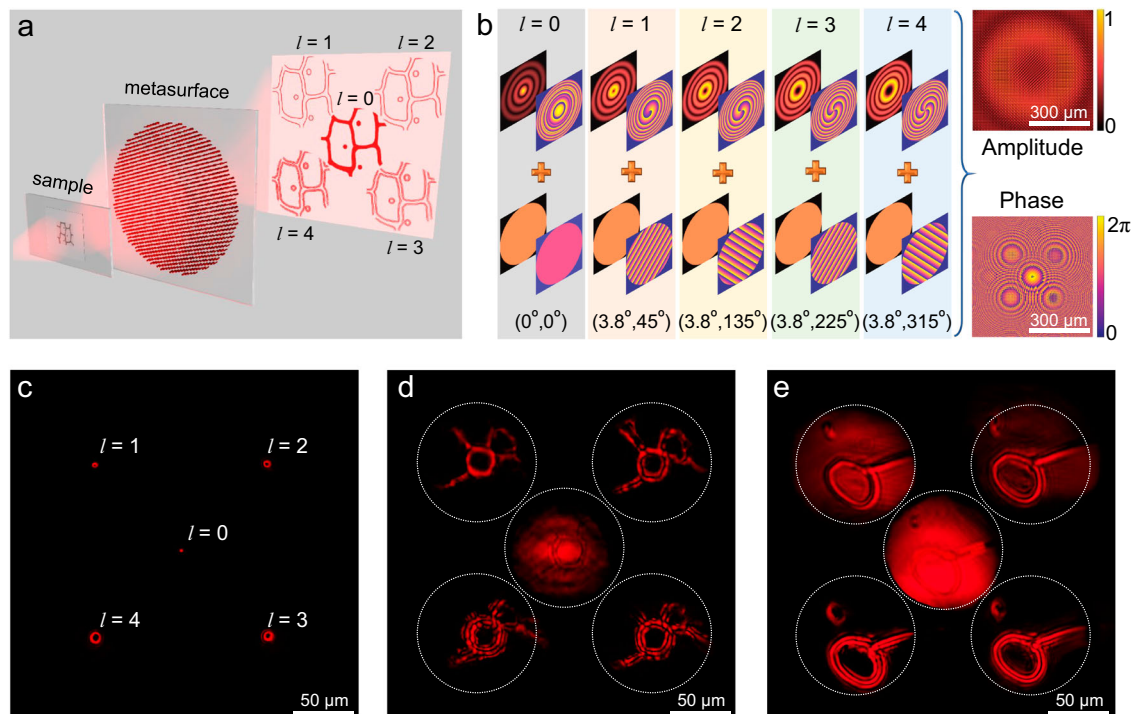


Fig. 5 | The integrated multichannel BVML for parallel processing. **a** Schematic illustration of the multichannel BVMLs synchronously performing the zeroth- to fourth-order differential operations. **b** The design flow and complex amplitude distributions of the multichannel BVMLs. Only the central region of the complex amplitude is presented at the right side to highlight the details. Scale bars: 300 μm .

c Experimentally measured PSF of the multichannel BVML at the wavelength of 633 nm. **d** Experimental imaging results for the unstained limewood stem cell as a phase object under the wavelength of 633 nm. **e** Experimental imaging results for the rough surface of transparent drop-casted ultraviolet adhesives under the wavelength of 633 nm. Scale bars of (c–e): 50 μm .

normalized to $1/5$. (ϕ_l, φ_l) are the designed polar angles and azimuth angles that determine the output position of each differential operation. The target complex amplitude distribution of the multichannel BVML can be obtained by preset (ϕ_l, φ_l) as described in Fig. 5b.

The multichannel BVML is fabricated using the same method as above, and the corresponding optical photograph is shown in Fig. S8. The fabricated device has a diameter of 1.2 mm and a focal length of 1.5 mm for all channels. We measure the intensity distribution of the PSF of the device under LCP coherent illumination at the wavelength of 633 nm, as depicted in Fig. 5c, and the broadband response is presented in Fig. S9. They agree very well with the simulation results (Fig. S10), and each PSF shows the same uniform distribution as the single-channel BVML recorded in Figs. 2f–i, which enables each channel in the designed multichannel BVML to perform the corresponding operation independently.

Then, we select the unstained limewood stem cell as the imaging specimen to verify the synchronous multi-order differential imaging functionality of the device. This specimen only significantly affects the phase, not its amplitude, and is thus referred to as a phase object. The experimental setup is the same as in Fig. 3a. Figure 5d shows the zeroth- to fourth-order differential images captured synchronously in five channels at the wavelength of 633 nm. The zeroth-order differential channel presents a traditional bright field imaging where the overall morphology of the specimen can only be vaguely observed, while the more critical shapes and boundaries of the internal cells cannot be clearly identified because of their transparency. Moreover, the first-order differential channel realizes rough edge detection of the specimen by blocking part of the low-frequency components. In contrast, the higher-order differential channel leads to more apparent peaks at the edges of the specimen, revealing more detailed information. This ability to capture rich details will undoubtedly facilitate applications in multicellular localization and classification.

In addition, we also notice that higher-order differential operations have more significant advantages in filtering out low- and mid-frequency components and, therefore, can exhibit a more substantial sharpening effect on the edges of the sample, especially for the objects with relatively smooth changes in amplitude and phase (See the detailed results in Figs. S11 and S12). For experimental verification, Fig. 5e records the imaging results for the rough surface of the transparent drop-casted ultraviolet (UV) adhesives. It is clear that the morphological information in the zeroth-order channel is completely submerged in the low-frequency background. The imaging results in low-order differential channels are also affected by part of the mid-low frequency components stemming from rough surfaces, resulting in the unremoved background and blurred outline. With the increasing order of the differential processing, the edges of the sample are gradually sharpened in the images. The higher-order differential channel shows more significant edge enhancement and higher contrast boundaries. All of the above differential operations are parallel, without the additional power consumption and the help of the image processing algorithm, thus opening up new opportunities for advanced imaging and optical analog computing.

Discussion

In summary, we propose and demonstrate a BVML based on a single-layer complex amplitude metasurface. By presetting the topological charge of the corresponding Bessel vortex, the designed BVMLs can perform multiple-order radial differential operations in the polar coordinate system, which enables two-dimensional optical analog signal processing. Leveraging the ultra-thin and flexible design of the metasurfaces, we synchronously implement the zeroth- to fourth-order radial differential processing of the input objects on a single device by angle multiplexing different information channels, demonstrating the superiority of the proposed BVMLs in parallel processing.

Therefore, we envision that the proposed compact and multi-functional BVMLs may have significant potential for application in the field of large-scale optical data processing and biomedical imaging.

Methods

Sample fabrication

The metasurface is fabricated using electron-beam lithography (EBL) on a 400 nm thick amorphous silicon (α -Si) film with quartz substrate to pattern the specific arrays. Firstly, an ARP6200 electron-beam resist layer is deposited by spin-coating on the α -Si film. Then, the sample is exposed through EBL, and the patterns are revealed after the development process. Afterwards, a 30 nm thick Aluminum layer working as the hard etching mask is deposited on the sample by electron-beam evaporator, and the lift-off process is done in N-Methylpyrrolidone (NMP). Next, the patterns are transferred to α -Si film by inductively coupled plasma (ICP) etching, where C_4F_8 and SF_6 are utilized during the etching process. The lower radio frequency (RF) power is 40 W, and the upper RF power is 500 W, the pressure being 13 mTorr. The ratio of C_4F_8/SF_6 is tuned to 2.5 to improve the anisotropy of etching effectively. Therefore, the final sample can be obtained after removing the Al hard etching mask.

Data availability

All the data in this study are provided within the paper and its supplementary information. The data of this study are available from the corresponding author upon request.

References

- Solli, D. R. & Jalali, B. Analog optical computing. *Nat. Photonics* **9**, 704–706 (2015).
- Woods, D. & Naughton, T. J. Photonic neural networks. *Nat. Phys.* **8**, 257–259 (2012).
- Lin, X. et al. All-optical machine learning using diffractive deep neural networks. *Science* **361**, 1004–1008 (2018).
- Kwon, H., Arbabi, E., Kamali, S. M., Faraji-Dana, M. & Faraon, A. Single-shot quantitative phase gradient microscopy using a system of multifunctional metasurfaces. *Nat. Photonics* **14**, 109–114 (2020).
- Li, C., Zhang, X., Li, J., Fang, T. & Dong, X. The challenges of modern computing and new opportunities for optics. *Photonix* **2**, 20 (2021).
- Wang, Z. et al. Single-layer spatial analog meta-processor for imaging processing. *Nat. Commun.* **13**, 2188 (2022).
- Fu, W. et al. Ultracompact meta-imagers for arbitrary all-optical convolution. *Light Sci. Appl.* **11**, 62 (2022).
- Umbaugh, S. *Computer Vision and Image Processing: A Practical Approach Using CVIPTools* (Prentice Hall PTR, 1998).
- Tang, H. et al. MRI brain image segmentation by multi-resolution edge detection and region selection. *Computerized Med. Imaging Graph.* **24**, 349–357 (2000).
- Rajab, M. I., Woolfson, M. S. & Morgan, S. P. Application of region-based segmentation and neural network edge detection to skin lesions. *Computerized Med. Imaging Graph.* **28**, 61–68 (2004).
- Franke, U. et al. Autonomous driving goes downtown. *IEEE Intell. Syst. Their Appl.* **13**, 40–48 (1998).
- Assidiq, A. A., Khalifa, O. O., Islam, M. R. & Khan, S. Real time lane detection for autonomous vehicles. In *2008 International Conference on Computer and Communication Engineering* 82–88 (IEEE, 2008).
- Qiang, C. & Wang, H. A real-time lane detection algorithm based on a hyperbola-pair model. In *2006 IEEE Intelligent Vehicles Symposium* 510–515 (IEEE, 2006).
- Oti, J. E., Canales, V. F. & Cagigal, M. P. The optical differentiation coronagraph. *Astrophys. J.* **630**, 631–636 (2005).
- Oti, J. E., Canales, V. F. & Cagigal, M. P. Analysis of the signal-to-noise ratio in the optical differentiation wavefront sensor. *Opt. Express* **11**, 2783–2790 (2003).
- Park, Y., Azaña, J. & Slavík, R. Ultrafast all-optical first- and higher-order differentiators based on interferometers. *Opt. Lett.* **32**, 710–712 (2007).
- Ngo, N. Q., Yu, S. F., Tjin, S. C. & Kam, C. H. A new theoretical basis of higher-derivative optical differentiators. *Opt. Commun.* **230**, 115–129 (2004).
- Zhang, W., Wang, Y., Xu, D., Luo, H. & Wen, S. All-optical differentiator in frequency domain. *Appl. Phys. Lett.* **120**, 011102 (2022).
- Silva, A. et al. Performing mathematical operations with metamaterials. *Science* **343**, 160–163 (2014).
- Zhou, J. et al. Two-dimensional optical spatial differentiation and high-contrast imaging. *Natl. Sci. Rev.* **8**, nwa176 (2020).
- Guo, C., Xiao, M., Minkov, M., Shi, Y. & Fan, S. H. Photonic crystal slab Laplace operator for image differentiation. *Optica* **5**, 251–256 (2018).
- Zhu, T. et al. Plasmonic computing of spatial differentiation. *Nat. Commun.* **8**, 15391 (2017).
- Zhou, Y., Zheng, H. Y., Kravchenko, I. I. & Valentine, J. Flat optics for image differentiation. *Nat. Photonics* **14**, 316–323 (2020).
- Kim, Y., Lee, G. Y., Sung, J., Jang, J. & Lee, B. Spiral metalens for phase contrast imaging. *Adv. Fun. Mater.* **32**, 2106050 (2022).
- Pahlevaninezhad, M., Huang, Y. W. & Pahlevani, M. Metasurface-based bijective illumination collection imaging provides high-resolution tomography in three dimensions. *Nat. Photonics* **16**, 203–211 (2022).
- Guo, Y., Zhang, S. & Pu, M. Spin-decoupled metasurface for simultaneous detection of spin and orbital angular momenta via momentum transformation. *Light Sci. Appl.* **10**, 63 (2021).
- Zhang, F., Pu, M. & Li, X. All-dielectric metasurfaces for simultaneous giant circular asymmetric transmission and wavefront shaping based on asymmetric photonic spin-orbit interactions. *Adv. Fun. Mater.* **27**, 1704295 (2017).
- Liu, M., Zhu, W. & Huo, P. Multifunctional metasurfaces enabled by simultaneous and independent control of phase and amplitude for orthogonal polarization states. *Light Sci. Appl.* **10**, 107 (2021).
- Schlickriede, C., Kruk, S. & Wang, L. Nonlinear imaging with all-dielectric metasurfaces. *Nano Lett.* **20**, 4370–4376 (2020).
- Wen, D., Cadusch, J. J., Meng, J. & Crozier, K. B. Vectorial holograms with spatially continuous polarization distributions. *Nano Lett.* **21**, 1735–1741 (2021).
- Zhou, J., Wu, Q. & Zhao, J. Fourier optical spin splitting microscopy. *Phys. Rev. Lett.* **129**, 020801 (2022).
- Zhao, M. et al. Optical phase contrast microscopy with incoherent vortex phase. *Laser Photon. Rev.* **16**, 2200230 (2022).
- Zhu, T. et al. Generalized spatial differentiation from the spin Hall effect of light and its application in image processing of edge detection. *Phys. Rev. Appl.* **11**, 034043 (2019).
- Zhu, T., Huang, J. & Ruan, Z. Optical phase mining by adjustable spatial differentiator. *Adv. Photonics* **2**, 016001 (2020).
- Zhu, T. et al. Topological optical differentiator. *Nat. Commun.* **12**, 680 (2021).
- Abdollahramezani, S., Chizari, A., Dorche, A. E., Jamali, M. V. & Salehi, J. A. Dielectric metasurfaces solve differential and integro-differential equations. *Opt. Lett.* **42**, 1197–1200 (2017).
- Zhou, Y. et al. Analog optical spatial differentiators based on dielectric metasurfaces. *Adv. Opt. Mater.* **8**, 1901523 (2019).
- Pan, D. et al. Laplace metasurfaces for optical analog computing based on quasi-bound states in the continuum. *Photon. Res.* **9**, 1758–1766 (2021).
- Cotrufo, M., Singh, S., Arora, A., Majewski, A. & Alù, A. Polarization imaging and edge detection with image-processing metasurfaces. *Optica* **10**, 1331–1338 (2023).
- Huo, P. et al. Photonic spin-multiplexing metasurface for switchable spiral phase contrast imaging. *Nano Lett.* **20**, 2791–2798 (2020).

41. Zhang, Y. et al. Dielectric metasurface for synchronously spiral phase contrast and bright-field imaging. *Nano Lett* **23**, 2991–2997 (2023).
42. Tanriover, I., Dereshgi, S. A. & Aydin, K. Metasurface enabled broadband all optical edge detection in visible frequencies. *Nat. Commun.* **14**, 6484 (2023).
43. Cordaro, A. et al. High-index dielectric metasurfaces performing mathematical operations. *Nano Lett* **19**, 12 (2019).
44. Cotrufo, M., Arora, A., Singh, S. & Alù, A. Dispersion engineered metasurfaces for broadband, high-NA, high-efficiency, dual-polarization analog image processing. *Nat. Commun.* **14**, 7078 (2023).
45. Liang, X. et al. All-optical multiplexed meta-differentiator for tri-mode surface morphology observation. *Adv. Mater.* **35**, 2301505 (2023).
46. Deng, M. et al. Broadband angular spectrum differentiation using dielectric metasurfaces. *Nat. Commun.* **15**, 2237 (2024).
47. Liu, Y., Huang, M., Chen, Q. & Zhang, D. Single planar photonic chip with tailored angular transmission for multiple-order analog spatial differentiator. *Nat. Commun.* **13**, 7944 (2022).

Acknowledgements

The authors acknowledge support from the Key Research and Development Program of the Ministry of Science and Technology of China (2022YFA1205000 to T.X. and 2022YFA1207200 to P.H.), National Natural Science Foundation of China (12274217 to T.X. and 62105142 to P.H.), the Natural Science Foundation of Jiangsu Province (BK20220068 to T.X. and BK20212004 to Y.L.) and the Fundamental Research Funds for the Central Universities (to T.X.). The authors acknowledge the technique support from the microfabrication center of the National Laboratory of Solid-State Microstructures.

Author contributions

P.H. and T.X. conceived the idea. Y.L. and T.X. supervised the project. P.H. and L.T. performed the theoretical verification, numerical simulations, experiments and data analysis. Y.J. contributed significantly to the fabrication process. Y.Z., M.L., P.L., S.Z., Y.W., and H.R. provided useful discussions and comments. P.H. and L.T. wrote the paper. T.X. revised the manuscript. All authors approved the manuscript.

Competing interests

The authors declare no competing interests.

Additional information

Supplementary information The online version contains supplementary material available at <https://doi.org/10.1038/s41467-024-53463-3>.

Correspondence and requests for materials should be addressed to Yanqing Lu or Ting Xu.

Peer review information *Nature Communications* thanks Bin Hu and the other, anonymous, reviewer(s) for their contribution to the peer review of this work. A peer review file is available.

Reprints and permissions information is available at <http://www.nature.com/reprints>

Publisher's note Springer Nature remains neutral with regard to jurisdictional claims in published maps and institutional affiliations.

Open Access This article is licensed under a Creative Commons Attribution-NonCommercial-NoDerivatives 4.0 International License, which permits any non-commercial use, sharing, distribution and reproduction in any medium or format, as long as you give appropriate credit to the original author(s) and the source, provide a link to the Creative Commons licence, and indicate if you modified the licensed material. You do not have permission under this licence to share adapted material derived from this article or parts of it. The images or other third party material in this article are included in the article's Creative Commons licence, unless indicated otherwise in a credit line to the material. If material is not included in the article's Creative Commons licence and your intended use is not permitted by statutory regulation or exceeds the permitted use, you will need to obtain permission directly from the copyright holder. To view a copy of this licence, visit <http://creativecommons.org/licenses/by-nc-nd/4.0/>.

© The Author(s) 2024